*Proceedings of the 4th International Conference on Frontiers of Design and Manufacturing, ICFDM'2000, Hangzhou*, China, June 17-19, 2000.

# RECENT DEVELOPMENT IN LASER MATERIALS PROCESSING

Y. Lawrence Yao, Wayne Li, and Kai Chen
Department of Mechanical Engineering, Columbia University, 220 Mudd Bldg., MC 4703
New York, NY 10027, USA

## ABSTRACT

Recent research and development in laser machining and laser forming processes is reviewed. In the laser machining area, striation formation and prediction, and gas jet - workpiece interactions are discussed. In the laser forming area, strain rate effects, and convex forming are presented.

## LASER MACHINING

### Striation Mechanism and Prediction

**1. Introduction**

The formation of periodic patterns (striation) has drawn much attention in laser cutting of mild steel since it strongly affects the quality of cut finish (Figure 1.1). The fluctuation of absorbed laser power during the laser beam and the gas flow interacting with the work-piece will bring about fluctuation of the molten front and in special cases, the liquid layer can oscillate with a natural frequency even without fluctuations in absorbed power (Schuocker, 1986). The high-speed gas jet during melt ejection will cause hydrodynamic instabilities of the molten front (Vicanek, *et al*., 1986). Arata *et al.* (1979) conducted a detailed experimental investigation about the molten front in the cutting process. They suggested that when the cutting speeds are less than the velocity of the reactive front, the ignition and extinction cycles of reaction begin to take place. But some reports indicate even the cutting speed is above the critical speed, striations still exist (Ivarson, *et al*., 1994, Di Pietro, *et al*., 1997). A cyclic oxidation model is further suggested (Ivarson, *et al*., 1994). For diffusion controlled reaction, the rate of chemical reaction is time dependent, being rapid in the early stages but decreasing markedly as the thickness of the oxide layer increases. So the oxide layer will expand rapidly at first but slow down afterwards. Once the oxide is blown out from the cutting front, due to a sudden decrease of the oxide layer, another expansion will begin. Although this model gives a quite convincing explanation on the expansion of the oxide layer, it does not clearly explain how the oxide layer is suddenly reduced. If one assumes that the melt removal is a continuous process, the oxidation cycle will not generate striation, because when the oxidation and melting speed is finally the same as the melt removal rate, the entire process will no longer be cyclic.

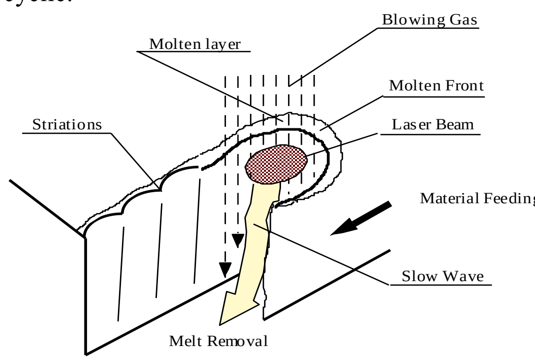


Figure 1.1 Schematic of oxygen cutting of mild steel (Chen & Yao, 1999)

**2. Physical Model of Melt Removal and Striation Formation**

The behavior of a thin liquid film under gas flow has been studied over decades. The behavior of the liquid film is largely dependent on the gas velocity, the liquid flow rate (or Reynolds number) and the film thickness. Ripples are generated on the surface when a high-velocity gas flows above a thick liquid layer, because the viscous dissipation is less than the energy transferred by the wave-induced pressure perturbation. The wave behavior depends on the gas velocity and the liquid flow rate. As the film thickness is reduced, the surface smoothes out because the friction in the liquid phase can overcome the pressure perturbation. As the film thickness is further reduced to a very small value, it is found that the liquid film becomes unstable because the wave-induced shear stress perturbation is sufficient to overcome the restoring forces, and so called slow waves are generated on the surface (Craik, 1966). It is perceivable that, if the liquid film gets even thinner and has a lower fluid flow rate, the film will rupture.

For the case of laser cutting of mild steel, it is commonly accepted that the molten front thickness is of the order of $10^{-5}$m (Vicanek, 1986; Arata, 1979). In such an order of thickness, the molten front is unstable and can easily rupture.

Consider the top part of the molten front (Figure 1.2). At low cutting speeds, the liquid film has relatively long exposure time in the gas flow and the liquid film will usually rupture since there is not enough liquid flow rate on the top part of the molten front. This phenomenon has been observed and described by Arata *et al.* (1979). When the cutting speed increases, the period of film rupture becomes shorter. At some critical cutting speed, there is not enough time for instabilities to develop causing film rupture, and there is always a liquid film on the top of the molten front. This was described by Arata *et al.* (1979) as “steady cutting”, which corresponds to a cutting speed above 2m/min. This thin liquid film for mild steel of certain thickness, however, may still be unstable and instead of film rupture, slow waves may be generated. Once the crest of the slow wave moves downwards from the top of the molten front, much more melt is removed and oxidation coupled with heat conduction begins to expand. The process is fast at first and slows down until another wave crest comes and moves the melt downwards. Thus an expansion-compression cyclic pattern is still formed above the so-called critical cutting speed.

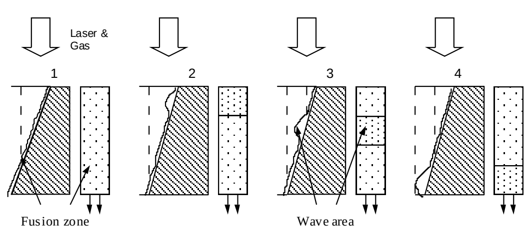


Figure 1.2 Schematic of the molten front change at high cutting speeds (Chen & Yao, 1999)

It has been shown by Makashev *et al*. (1993) that a steady flow of the melt layer on the upper edge is impossible. Instead of wave generation, they proposed that a melt drop will quickly grow up to a critical size and then move down. Their theory of droplet formation on the upper edge is not convincing enough, because the liquid flow rate is very small and the liquid layer is basically in laminar state (it is estimated that the liquid Re number is comparable to 1). Moreover, as mentioned earlier, there is not enough time for film rupture when cutting speed is high. Vicanek *et al.* (1986) treated the melt flow as a two-dimensional boundary layer and gave the stationary thickness of the molten layer along with an instability analysis. The stress perturbation, however, was not considered in their approach and hence the results are not accurate enough to give a quantitative description of the striation pattern.

## 3. Theoretical Background

The analysis of the instabilities generated on a liquid film by an adjacent high speed gas jet begins with the linearized Navier-Stokes equations of the liquid film. Only two-dimensional harmonic disturbances are considered here (Figure 1.3).

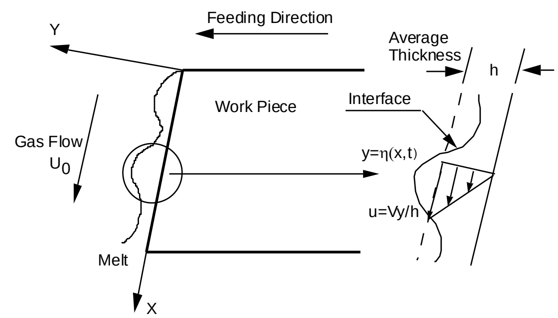


Figure 1.3 Schematic of shear flow and surface disturbance (Chen & Yao, 1999)

The two-dimensional treatment will reveal the basic nature of the problem, since every periodic three-dimensional disturbance may be represented in terms of a corresponding two-dimensional problem. A detailed mathematical treatment can be found in Chen & Yao, (1999).

Instability occurs when the surface stress is sufficiently large to overcome the restoring forces of surface tension, that is:

$$P_r + \frac{3T_i}{2kh} \geq \gamma k^2 h\,, \tag{1}$$

where $P_r$ is normal stress parameter $T_i$ tangential stress parameter, $k$, wave number, $h$ liquid film thickness, and $\gamma$ surface tension. For the case of laser cutting, the condition that (kh)R is small is satisfied, where $R$ is Reynolds number of liquid. In the case of small film thickness, the shear force perturbation will be dominant, the Eq. (1) can be further simplified as:

$$h < \left(\frac{3T_i}{2\gamma k^3}\right)^{1/2}. \tag{2}$$

In the aforementioned physical model, the striation frequency is equivalent to the oscillation frequency of melt ejection and oxidation. Under high speed cutting conditions, the frequency should be equivalent to the slow wave frequency. The wave number of the slow wave is approximately taken as the critical wave number at which the mean shear stress $\tau$ attains the minimum value. Undamped disturbances for the liquid film of thickness h are sustained at such a minimum value. Substituted by the proper stress evaluation, Eq. (1) becomes

$$\frac{I}{c_f}[\frac{k\tau}{\rho}+\frac{3\beta v^{2/3}}{2h}(\frac{k\tau}{\rho})^{2/3}]=\frac{\gamma k^2}{\rho}. \qquad (3)$$

where $c_f$ is friction factor, $\rho$ density of the melt, and $v$ liquid velocity in y direction (Figure 3) or cutting.

Taking derivative $\partial\tau/\partial k$ of the above equation, one obtains the positive critical wave number:

$$k=\frac{I\tau}{4c_f\gamma}. \qquad (4)$$

where $\tau$ mean shear stress, which is evaluated according to

$$\tau=\mu\frac{V}{h}. \qquad (5)$$

where $\mu$ is viscosity of the melt, and $V$ interfacial velocity. Theoretical result show that the wave speed is equal to the interfacial velocity. However, the experimental measurements show that the wave speed is actually less than the interfacial velocity. A reasonable approximation is obtained by considering a coefficient of, say, 0.8 (Craik, 1966), $c$=0.8$V$, where c is the wave velocity and V the interfacial velocity. This takes into account the non-linear effects which may reduce the wave velocity. Thus we can use $V$ calculated to approximate wave velocity. The wave frequency is then

$$f = 0.8Vk/2\pi. \qquad (6)$$

As discussed in the physical model section, the wave frequency is actually the frequency of the striation. The striation wavelength is, however, a combination of striation frequency and the cutting speed $v$

$$\lambda = v/f. \qquad (7)$$

The interfacial velocity $V$ is dependent on the stationary liquid film thickness $h$, which should be derived from steady state energy and momentum balance. The calculation method from Vicanek *et al*. (1986) is used to obtain the values of film thickness $h$ as a function of cutting speed and gas velocity. They treated the molten front as a plane and solved the momentum equations based on boundary theory, taking the physical properties at the wall temperature instead of solving the energy equation.

As mentioned in the introductory section, striation formation has been found to be strongly related to oxidation in laser cutting. The exothermic oxidation typically contributes nearly half of the total energy input. The oxidation equation can be written as

$$\frac{ds}{dt}=A(p_0)\frac{\exp(-T_0/T)}{s(t)}, \qquad (8)$$

where $A$ is a coefficient which has presumably a linear relationship with the oxygen pressure $p_o$ at the surface of the molten front. $T_0$ is the activation temperature for the diffusion. An estimate for the oxide layer thickness $s$ can be achieved by neglecting temperature variation and simply integrating Eq. (8) to give the well-known parabolic equation:

$$s_m^2 = A(p_0)t_p, \qquad (9)$$

where $s_m$ is the maximum thickness of the oxide layer. The time period $t_p$ is the inverse of frequency from Eq. (6). If one calculates the striation frequency from Eq. (6), the maximum depth of the striations can be estimated from Eq. (9) if the coefficient is experimentally calibrated. More detailed treatment of oxidation can be found in Chen, Yao, and Modi (1999a)

## 4. Calculation and Experimental Results

Experiments were carried out for oxygen assisted cutting of 1.6 mm thick steel 1018 with a $CO_2$ laser. The laser power used is 500 W, gas pressure 2.1 bar, and cut speed varied from 15 to 50 mm/s. The striation wavelength and depth are obtained from Talysurf profiles taken from a position 0.5 mm from the top of the cut edge.

The predicted striation wavelength and the experimental results are given in Figure 1.4 and they are in agreement. The increase in cutting speed causes the liquid film thickness and thus the interfacial velocity to increase. As a result, the striation frequency increases, but not as much as the increase of the cutting speed. The net result, therefore, is that the striation wavelength increases with the cutting speed.

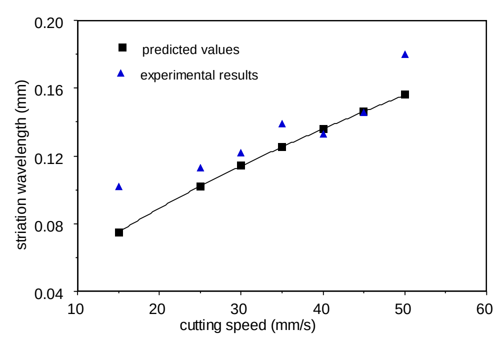


Figure 1.4 striation wavelength versus cutting Speed (Chen & Yao, 1999)

Striation depth is evaluated using Eq. (9). This assumes that the parabolic growth of the oxide layer is directly related to the striation depth. Figure 1.5 shows the predicted maximum striation depth against the experimental measurements. The coefficient in Eq. (9) is calibrated to be a constant of $4x10^{-8}$. The increase of the striation frequency with the cutting speed gives a shorter interaction period for the oxidation and the melting process, thus reduces the striation depth. The prediction is consistent with the experimental results.

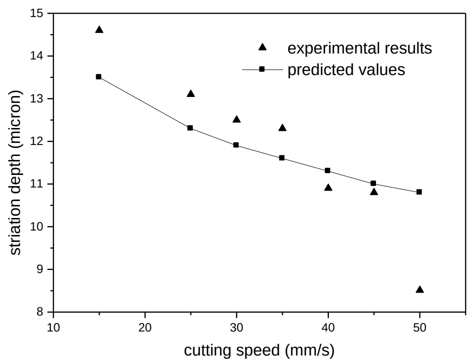


Figure 1.5 maximum striation depth versus cutting speed (Chen & Yao, 1999)

**5. Conclusions**

A theory of the unstable characteristic of the melt ejection combined with the oxidation oscillation is proposed to explain the mechanism of the striation generation. When the cutting speed is small, the liquid film ruptures on the cutting front. When the cutting speed increases to a some point, waves are produced on the top of the cutting front in place of film rupture. Each of the wave crest or film rupture results in a sudden increase of the melt removal and thus the acceleration of the oxidation and the melting. As a result, a cyclic pattern is formed on the cut edge. The striation frequency is related to the frequency of the slow waves or film rupture. The calculated striation frequency (or wavelength) matches the experimental results. The maximum depth of the striation pattern is predicted along with the temperature fluctuation range at the molten front and they show similar trend. The predicted tendencies are consistent with the experimental results.

## Gas jet - Workpiece Interactions

**1. Introduction**

The assist gas plays an important role in laser machining. It provides a mechanical force to eject the melt from the cut zone and cools the cut zone by forced convection. Inefficient removal of the molten layer can lead to machining surface deterioration. When the gas is reactive, it also delivers additional exothermic energy to assist in machining.

The role of oxygen pressure in laser cutting of steels was studied experimentally by Ivarson *et al*. (1996). They found that there are two optimum pressure ranges where the cut quality is good. Numerical calculations of the three-dimensional turbulent oxygen jet by O'Neill and Steen (1996) showed that entrainment of impurities occurs inside the cut kerf and this can have detrimental effects on oxidation and cutting capability. The use of an off-axis nozzle in tandem with a coaxial nozzle was investigated by Chryssolouris and Choi (1989), and the use of a single off-axis nozzle was studied experimentally by Brandt and Settles (1997). Other supersonic nozzle configurations have also been considered to improve the effects of gas jet (O'Neill, *et al*., 1992, Man, *et al*., 1997). A comprehensive review of the gas jet effects was presented by Fieret *et al* (1987), in which a Mach shock was found to reduce the stagnation pressure at the workpiece and to encourage the formation of a stagnation bubble on the surface of the workpiece.

In industrial practice, nozzles are positioned close to the workpiece and nozzle pressures are chosen within a certain range. There is however little theoretical work to systematically study the effects of a gas jet and process parameters such as nozzle position and gas pressure.

The current effort aims at examining the gas jet effects by carrying out numerical simulations and experiments in a geometry that closely mimics the real machining case. Simulations are first validated against several well-documented free jet and impinging jet cases, for which experimental data exists. The validity of the simulation results is further supported by the experimental investigation.

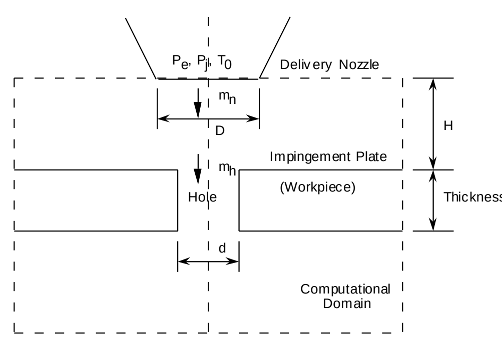


Figure 2.1 Schematic of computational domain for simulation (Chen, Yao & Modi, 1999b)

This study primarily utilizes an axisymmetric geometry in which a through hole on the impinging plate is made concentric with the nozzle axis (Figure 2.1). Axisymmetric studies have significance not only because they corresponds to the laser drilling case, but because they also reveal the generic behavior of the gas flow upstream of the machining front. This flow behavior is expected to be relatively independent of the actual cut geometry.

The gas flow structure and the mass flow rate through the hole are primarily determined by the total pressure upstream of the hole, while in turn is primarily determined by the shock structure. Although melting and vaporization are important in laser machining, they are less likely to adversely affect the structure upstream of the hole and therefore are not considered. As will be shown below, these assumptions are found to be reasonable via agreement of experimental and simulated mass flow rate as well as laser machining experiments.

## 2. Numerical Simulations

A conical convergent nozzle is assumed to deliver a gas jet that normally impinges onto a workpiece plate with a through hole concentric with the nozzle (Figure 2.1). The through hole diameter $d$ is assumed to be smaller than the exit diameter of nozzle $D$.

The flow is assumed to be governed by the steady compressible Reynolds-Averaged Navier-Stokes (RANS) equations. A two-equation $k$-$\varepsilon$ turbulence model for turbulent kinetic energy ($k$) and energy dissipation ($\varepsilon$) based on the Renormalization Group (RNG) theory is utilized. In axisymmetric coordinates the RANS equations can be written as

$$\frac{\partial(F-F_v)}{\partial x}+\frac{\partial(G-G_v)}{\partial r}=0\,, \qquad (10)$$

In the above form ($F$, $G$) and ($F_v$, $G_v$) represent the inviscid and viscous flux terms respectively.

$$F=r\begin{bmatrix}\rho u\\ \rho u^2+p\\ \rho uv\\ (\rho e+p)u\end{bmatrix},\ G=r\begin{bmatrix}\rho v\\ \rho uv\\ \rho v^2+p\\ (\rho e+p)v\end{bmatrix},$$

$$F_v=r\begin{bmatrix}0\\ \tau_{xx}\\ \tau_{xr}\\ u\tau_{xx}+v\tau_{xr}\end{bmatrix},\ G_v=r\begin{bmatrix}0\\ \tau_{xr}\\ \tau_{rr}\\ u\tau_{rx}+v\tau_{rr}\end{bmatrix}. \qquad (11)$$

The stress terms in axisymmetric coordinates are

$$\tau_{xx}=\mu[2\frac{\partial u}{\partial x}-\frac{2}{3}(\frac{1}{r}\frac{\partial}{\partial r}(rv)+\frac{\partial u}{\partial x})]\,,$$

$$\tau_{rr}=\mu[2\frac{\partial v}{\partial r}-\frac{2}{3}(\frac{1}{r}\frac{\partial}{\partial r}(rv)+\frac{\partial u}{\partial x})]\,,$$

$$\tau_{xr}=\tau_{rx}=\mu[\frac{\partial u}{\partial r}+\frac{\partial v}{\partial x}]\,. \qquad (12)$$

The effective viscosity $\mu$ is composed of the molecular viscosity $\mu_m$ and the turbulent viscosity $\mu_t$, i.e. $\mu=\mu_m+\mu_t$, and is obtained from RNG theory:

$$\mu=\mu_m[1+\sqrt{\frac{C_\mu}{\mu_m}}\frac{k}{\sqrt{\varepsilon}}]^2\,. \qquad (13)$$

where $C_\mu$ is a constant. The density and the total internal energy assuming ideal gas behavior are

$$e=\frac{p}{\rho(\gamma-1)}+\frac{1}{2}(u^2+v^2)\text{, and } \rho=\frac{p}{RT}\,. \qquad (14)$$

The equations and relationships outlined in the section provide a set of equations with the primary variables of $\rho$, $p$, $u$, $v$, $k$ and $\varepsilon$. A commercial computational fluid dynamic (CFD) code, RAMPANT is used to solve these equations. More detailed treatment can be found in Chen, Yao and Modi (1999b).

## 3. Model Experimental Setup

The model experimental setup was designed to measure the mass flow rate through a predrilled hole in a plate (workpiece) with variation of total nozzle pressure and standoff distance. While the mass flow rate through the cut kerf may not be of concern in itself for laser machining, it is directly related to the total pressure at the machining front which in turn is an important factor in determining the material removal capability of the gas jet. The measurement of the mass flow rate also provides a convenient and viable verification of the simulation results. Considering the small physical dimension of the actual laser kerf, field measurement of the flow would be very difficult.

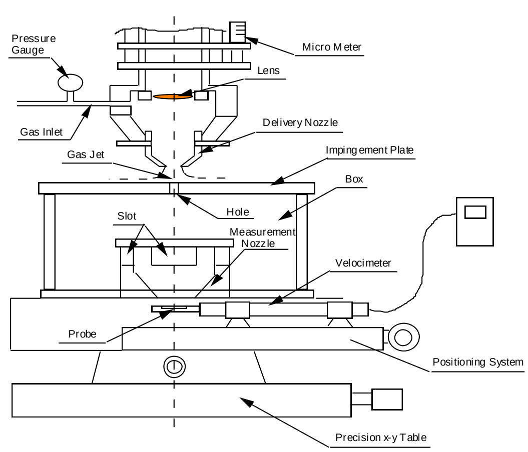


Figure 2.2 Schematic of experiment setup (Chen, Yao & Modi, 1999b)

A schematic of the experimental setup is shown in Figure 2.2. A commercial sonic (converging-only) nozzle with a nozzle diameter $D$ of 1.35mm is used. Compressed air from a gas tank is fed into the nozzle through a gas inlet where a pressure gauge was set. The gas exiting the nozzle impinges on an plate (or workpiece) with a predrilled hole in it. The impingement plate is 1.5mm thick with two through holes (with diameters 0.508mm or 0.711mm). The nozzle flow $\dot{m}_n$ is in part deflected by the plate. The remaining flow, through hole flow $\dot{m}_h$ enters the hole. The small hole diameter and the high gas speeds make it difficult to measure the through flow. Hence a collection box is placed directly underneath to collect the flow and direct it to a 10mm measurement nozzle (area $A_m$ = 78.5 mm$^2$) at considerably lower flow speed. The velocity of the gas leaving the measurement nozzle ($V_m$) is then measured using a hot-film anemometer (TSI 8350). The hot-film probe is placed directly underneath the measurement nozzle exit. The measurement nozzle contour guarantees that the velocity profile of the gas steam is nearly uniform. The density of the gas leaving the measurement nozzle $\rho_m$ is assumed to be that of an ideal gas at ambient conditions. The mass flow rate through the measurement nozzle ($\rho_m A_m V_m$) and hence the through hole flow $\dot{m}_h$ is obtained.

## 4. Mass Flow Rate Experimental and Simulation Results

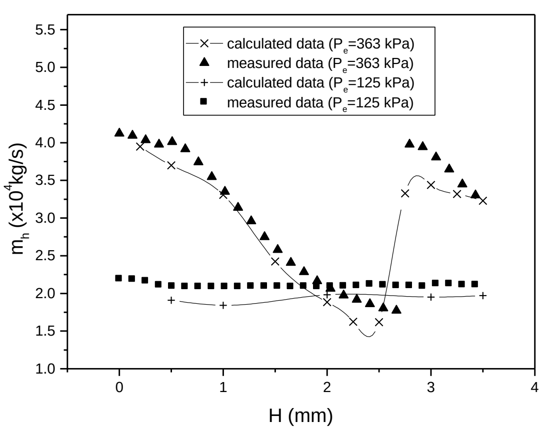


Figure 2.3 Computed and measured through hole mass flow rate for d = 0.711mm (Chen, Yao & Modi, 1999b)

The objective of the experimental part of this study was to determine the effects of hole diameter $d$, standoff distance $H$ and total pressure $p_t$ on the hole through flow $\dot{m}_h$. Three distinct values of $P_e$ were chosen and $H$ was varied continuously from 0 to 3.5mm for d = 0.711 mm.

Figure 2.3 shows the measured and simulated $\dot{m}_h$ data. At $P_e$ values of 125 kPa, $\dot{m}_h$ is relatively unaltered with changes in $H$, indicating that the flow structure remains unchanged along the centerline.

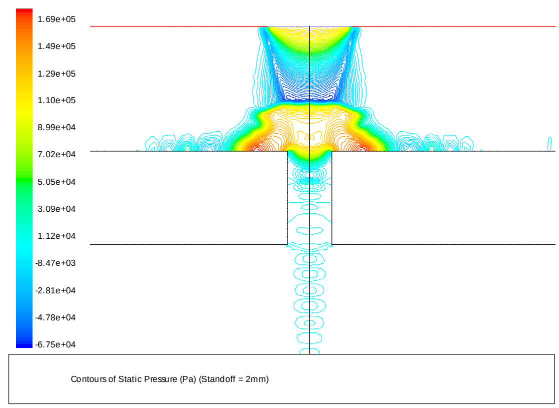


(a)

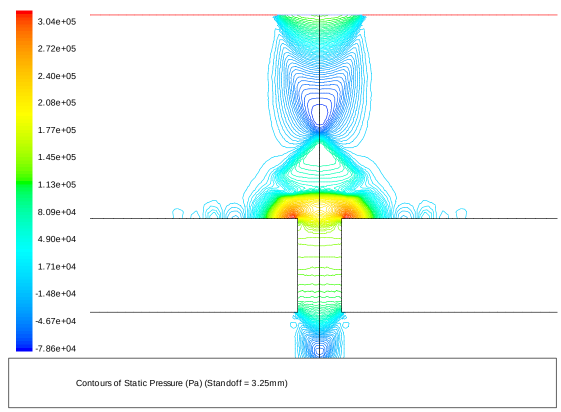


(b)

Figure 2.4 Contour of static pressure for (a) H = 2mm and (b) H = 3.25mm (d = 0.711mm, $P_e$ = 363 kPa) (Chen, Yao & Modi, 1999b)

However, for a higher $P_e$ value of 363 kPa, $\dot{m}_h$ reduces continuously until a critical standoff distance, $H_{critical}$ of about 3 mm is reached. At $H_{critical}$ a small increase in standoff distance results in a large jump in $\dot{m}_h$. Beyond this point $\dot{m}_h$ continues to decrease with increasing $H$. The critical point is accompanied with strong shock noises heard during the experiments. Good agreements between measured and simulated results are seen. The simulations were carried out over the computational domain shown in Figure 2.1 for the same operating pressure conditions as the experiments.

To further understand the particular phenomena seen in Figure 2.3, Figures 2.4a and 2.4b show the contours of static pressure for $H$ = 2 and 3.25mm, corresponding to two standoff distances before and after the jump in $\dot{m}_h$ seen in Figure 3 with $P_e$ of 363 kPa. In Figure 2.4a ($H$ = 2.0mm), the incident shock interacts with the normal standoff shock directly. For low values of $H$, the through-hole mass flow rate decreases as the standoff distance increases as long as the incident shock directly meets the standoff shock. However, when the standoff distance reaches a point where the incident shock waves first meet at the centerline before they reflect and interact with the normal shock, the loss of total pressure is greatly reduced, which results in a jump of the through-hole mass flow rate (Figure 2.4b).

In most laser machining cases, the nozzle standoff distance is chosen to be 0.5 to 1.5mm, thus the incident shock will always interact with the standoff shock directly.

The axisymmetric study shows that the material removal capability, represented by through-hole mass flow rate is directly affected by the shock structure. The shock structure, however, can be altered by variation of operating parameters such as gas pressure and standoff distance. Unlike the idealized axisymmetric case, the linear kerf of laser cutting renders the problem three-dimensional. Since the geometric size of the kerf width is much smaller than the nozzle diameter and hence the actual cut geometry will not significantly alter the shock structure upstream of the workpiece, it is expected that shock structure in real cutting will be similar to that of the axisymmetric case. This is confirmed in laser machining experiments.

**5. Laser Machining Experiment**

To verify the gas jet effects on laser machining quality, laser-cutting experiments were performed. Experiments were carried out under the same conditions of the mass flow rate experiments. Cold-rolled mild steel of 1.6 mm thickness was cut using a PRC-1500 $CO_2$ laser system operated in CW and $TEM_{00}$ mode. Air was used as assist gas for cutting, $P_e$ was fixed at 363 kPa, cutting speed 37 mm/s, laser power 800 W, and $H$ was varied from 0.5 to 3.5 mm.

Under the condition, various amount of dross was found clinging to the bottom edge of the cut kerf because air was used as assist gas (Fig. 2.5). Dross increases from $H$ = 1.0 to 1.5 mm. Cuts were incomplete at $H$ = 2.0 and 2.5 mm which is equivalent to extremely severe dross attachment. The dross attachment then suddenly decreases to a minimum amount at $H$ = 3.0 mm, and it increases slightly at $H$ = 3.5 mm. The sudden decrease of the dross corresponds to the jump of the mass flow rate at $P_e$ = 363 kPa as seen from Fig. 2.3.

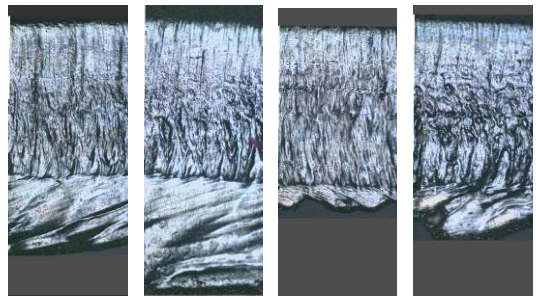

H=1.0mm 1.5mm 3.0mm 3.5mm

Figure 2.5 Dross attachment on cut surface with different standoff (incomplete cuts for H = 2.0 and 2.5 mm) ($P_e$ =363 kPa) (Chen, Yao, & Modi, 1999b)

As pointed out previously, the mass flow rate is directly affected by the shock structure which is primarily determined by the interactions between the nozzle, workpiece and gas flow. It is seen from the laser cutting experiments that a higher mass flow rate results in better material removal capability, thus better cut quality, whereas a significant drop in mass flow rate is responsible for larger dross attachment and poorer surface finish.

**6. Conclusions**

The numerical simulation of a transonic, turbulent jet impinging on a plate (workpiece) with a hole concentric with the jet is presented and the effects of gas pressure and nozzle standoff distance on shock structure is quantified. Experimental measurements of the mass flow rate through the hole under similar conditions agree with the simulation results. It is found that the total pressure loss across shocks depends on the shock structure. The shock structure is affected by the operating parameters of gas pressure and standoff distance. Under certain circumstances, the total pressure loss across the standoff shock is reduced leading to a higher through-hole mass flow rate, an indicator of a better material removal capability. The experimental results of laser machining confirm that the machining quality including roughness and dross attachment are affected by the shock structure and by subsequent mass flow rate (removal capability) as predicted.

## LASER FORMING

## Strain Rate Effects

## 1. Introduction

Laser forming is a process in which laser-induced thermal distortion is used to form sheet metal without a hard forming tool or external forces. It is therefore a flexible forming technique suitable for low-volume production and/or rapid prototyping of sheet metal, as well as for adjusting and aligning sheet metal components (Magee, et al., 1998). Aerospace, shipbuilding, microelectronics and automotive industries have shown interest

A simple type of the laser forming is straight-line laser bending (Fig.1) and more involved shapes can also be generated by the process.

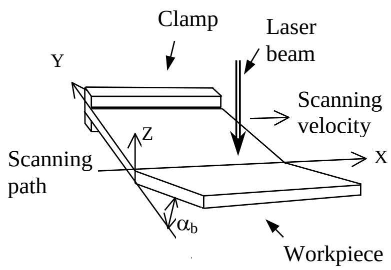


Fig. 3.1 Schematic of straight-line laser forming (Li & Yao, 1999)

Understanding various aspects of laser forming is a challenging problem of considerable theoretical and practical interest. Experimental and theoretical investigations have been reported to understand the mechanisms involved in laser forming. The proposed mechanisms are the temperature gradient mechanism (TGM) (Vollertsen, 1994a), buckling mechanism (BM) (Arnet and Vollertsen, 1995), and upsetting mechanism depending on operation conditions, material properties and workpiece geometry. A number of analytical models were derived to predict the bending angle $\alpha_b$ (Fig. 3.1) in the straight-line laser bending (Vollertsen, 1994b). Some of the models are in reasonable agreement with experimental results. More detailed studies were conducted via numerical investigations. Vollertsen, et al. (1993), Hsiao, et al. (1997), and Alberti, et al. (1994) simulated the process using the finite element or finite difference method. Parametric studies of process parameters, workpiece geometry and material properties on the laser forming process were reported, such as influence of strain hardening (Sprenger, et al., 1994), and edge effects (Magee et al., 1997, and Bao and Yao, 1999). Issues of working accuracy (Hennige, et al., 1997), and aerospace alloy application have also been reported.

The effects of strain rate in the laser forming, however, have not been studied in detail. Temperature in the laser forming could rise close to the melting point. As known, the strain rate at elevated temperatures has much higher influence on the material flow stress than at lower temperatures. The influence on the flow stress translates to that on the forming process and properties of the formed parts, including residual stresses and hardness of the formed parts.

Increasing scanning velocity only or increasing the velocity under the condition with constant ratio of laser power to the velocity can obtain results that is the combination of the effects of strain rate and input energy (Li and Yao, 1999). Therefore, the ideal scenario is to ensure the *net* energy input available for the forming purpose constant while the strain rate is varied. In this way the strain rate effects can be isolated and studied without interference of other variables. In this work, strain rate effects in laser bending are studied under the condition of "constant peak temperature," that is, the combinations of laser power and scanning velocity are so determined that the peak temperature reached at the top surface of the laser scanned workpiece remains constant. A numerical model based on the finite element method is developed to aid the determination of the process parameter values that give the constant peak temperature. The same model is also used to predict the effects of strain rate on bending angle and residual stress among others. The numerical results are experimentally validated.

## 2. Strain Rate and Effects

The stress and strain tensor, $\sigma_{ij}$ and $\varepsilon_{ij}$, can be decomposed into their mean portions and their deviatoric portions, that is, $\sigma = \sigma_{ii}/3$, $\varepsilon = \varepsilon_{ii}/3$, $s_{ij} = \sigma_{ij} - \delta_{ij}\sigma$, and $e_{ij} = \varepsilon_{ij} - \delta_{ij}\varepsilon$, where $\sigma$ and $\varepsilon$ are mean portion, $s_{ij}$ and $e_{ij}$ are deviatoric portions, and $\delta_{ij}$ is the Kronecker delta. For work-hardening materials, the relationship between deviatoric stress and plastic strain rate $\dot{e}_{ij}{}^{pl}$ by taking into consideration of temperature influence can be written in terms of tensor[10].

$$\dot{e}_{ij}{}^{pl} = 0, \qquad \text{if } f < 0, \text{ or if } f = 0 \text{ and } \left( \frac{\partial f}{\partial s_{ij}} \dot{s}_{ij} + \frac{\partial f}{\partial T} \dot{T} \right) < 0$$

$$\dot{e}_{ij}{}^{pl} = -\frac{1}{\dfrac{\partial f}{\partial e_{ij}{}^{pl}}} \left( \frac{\partial f}{\partial s_{kl}} \dot{s}_{kl} + \frac{\partial f}{\partial T} \dot{T} \right) \tag{15}$$

$$\text{if } f = 0 \text{ and } \left( \frac{\partial f}{\partial s_{ij}} \dot{s}_{ij} + \frac{\partial f}{\partial T} \dot{T} \right) \geq 0$$

For a one-dimensional deformation process of metals with a strain rate, $\dot{\varepsilon}$ , and temperature, *T,* the stress, $\sigma$, is given by

$$\sigma = C' \dot{\varepsilon}^m e^{\frac{mQ}{RT}} = C\dot{\varepsilon}^m \qquad (16)$$

where $m$ is the strain-rate sensitivity exponent, $Q$ the activation energy , $R$ the gas constant, both coefficient $C$ and $m$ depend on temperature and material.

### 3. Numerical Simulation

To simulate the strain rate effects in laser forming, reasonable values of the strain-rate sensitivity exponent $m$ and flow stress at different temperatures were obtained from available literature. Work hardening was also taken into consideration. The simulation of the laser forming process was realized by a thermal-structure analysis using commercial finite element analysis code ABAQUS. For thermal and structural analysis, the same mesh model is used. A user-defined FORTRAN program was necessary to model the heat source input from the Gaussian laser beam.

The main assumptions used in the numeral simulation of laser forming are as follows. The materials simulated in this work are isotropic and continuous. Plastic deformation generated heat is small as compared to energy input in the laser forming so that it is negligible. During the entire laser forming process, no melting takes place. The forming process is symmetrical about the laser-scanning path (Fig. 3.1).

The boundary conditions used include that the top surface is cooled by a weak gas flow. The remaining surfaces are cooled through free convection with atmosphere. Across the symmetric plane (the X-Z plane in Fig. 3.1), the movement of materials does not occur. The symmetric surface is under the adiabatic condition. Surface heat flux follows $q = q(\underline{x}, t)$, surface convection $q = h(T - T^o)$, where $h = h(\underline{x}, t)$ is the film coefficient, and $T^o = T^o(\underline{x}, t)$ the surrounding temperature, and radiation $q = A((T - T^z)^4 - (T^o - T^z)^4)$, where $A$ is the radiation constant and $T^z$ the absolute zero on the temperature scale used.

### 4. Experiment

To approximate the scenario, a constant peak temperature method was devised. Listed in Table 1 are values determined for a targeted peak temperature of 1,030°C.

Table 1 Experimental and simulation condition under constant peak temperature

| Velocity (mm/s) | 80 | 90 | 100 | 110 | 120 | 140 | 170 |
|---|---|---|---|---|---|---|---|
| Power (W) | 800 | 843 | 886 | 929 | 970 | 1040 | 1130 |

Laser bending experiments were carried out with a PRC1500 $CO_2$ laser system with the maximum power of 1.5 kW. The distribution of the power density is Gaussian ($TEM_{00}$). The diameter of the laser beam used is 4mm, which is defined as the diameter at which the power density becomes $1/e^2$ of the maximum power value. The samples were made of low carbon steel AISI 1010 and 80 mm by 40 mm by 0.89 mm in size, with 40 mm along the scanning direction. The samples were first cleaned using propanol and then coated with graphite coating to obtain relatively known and increased coupling of laser power. The geometry of the samples was measured before and after laser forming using a coordinate measuring machine. During the laser scanning, the samples were clamped at one side (Fig. 3.1). The residual stress was measured using X-ray diffractometry

### 5. Results and Discussion

As seen from Fig. 3.2, for the specified velocities, the laser power levels were determined via the simulation to give approximately the same peak temperature of 1,030°C at the top surface of workpiece (Table 1).

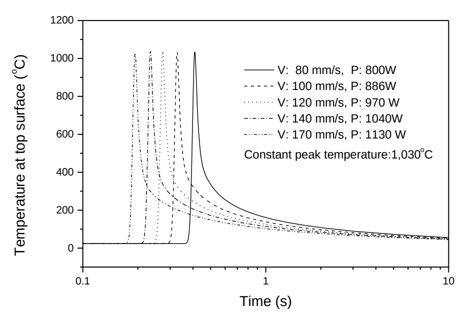


Fig. 3.2 Simulated time histories of temperature at the top surface under the condition of constant peak temperature (Li and Yao, 1999)

Fig. 3.3 compares the simulation and experimental results of the bend angle vs. velocity. In Fig. 3.4, a comparison of numerical simulation and experimental results is made for the Y-axis residual stress on the top surface of the workpiece. The yield stress of the material used at room temperature is about 265 MPa. When the strain rate is nearly doubled between the lower and higher speed cases, the residual stress increases by about 15%. In both figures, the simulation results agree with experimental measurements. The trends, namely, the bend angle decreasing and residual stress increasing with the increase of scanning velocity (strain rate) are consistent with the understanding of the forming mechanisms. Shown in Fig. 3.3 in a dotted line is the predicted bending angle without considering the strain rate effects. The predicted bending angle is larger without considering the strain rate effects obviously because the increase in the flow stress due to strain rate was left out and therefore larger deformations were predicted.

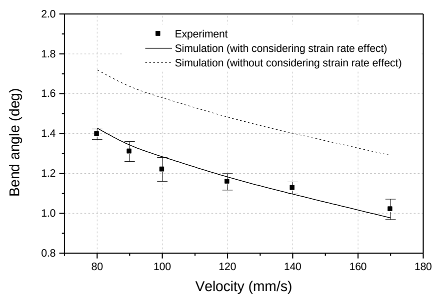


Fig. 3.3 FEM and experimental bend angle under the condition of constant peak temperature (Li and Yao, 1999)

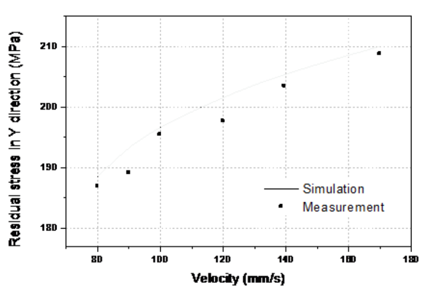


Fig. 3.4 FEM and X-ray diffraction measurement of residual stress for the samples scanned under the condition of constant peak temperature (Li and Yao, 1999)

Fig. 3.5 shows that, as the scanning velocity increases, the compressive plastic deformation at top surface becomes smaller. This is obviously due to the increase in strain rate associated with the increased velocity. The increased strain rate in turn causes the increase in flow stress, which makes bending more difficult at the increased velocity. It can be obtained that the bend angle decreases about 30% for the nearly doubled strain rate.

The hardness of the deformed workpiece is measured at the top surface along the scanning path (Fig. 3.6). The measurement is taken 6 days after the forming is done. As seen, the hardness decreases with the increase of velocity (shown in brackets), because of the effect of work hardening. At lower velocities, the strain rate and thus flow stress is lower, resulting in higher plastic strain. The higher plastic strain leads to more significant work hardening. A simple calculated relationship between the hardness and plastic strain is also superposed on Fig. 3.6 that agrees with the measurement data. The calculation is based on the well known empirical relationship between stress and hardness as well as $\sigma = K' \varepsilon^n$, where $\varepsilon$ is the simulated plastic strain, $n$ the work-hardening exponent for low carbon steel, and $K'$ constant.

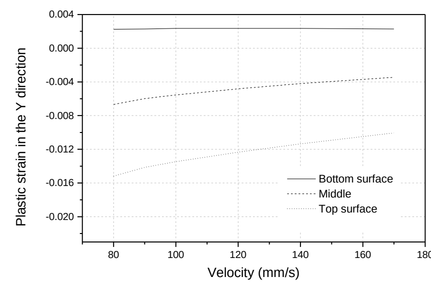


Fig. 3.5 Simulated plastic strain in Y direction under the condition of constant peak temperature (Li and Yao, 1999)

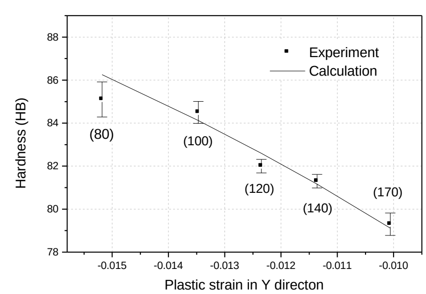


Fig. 3.6 Hardness vs. simulated plastic strain in Y direction under the condition of constant peak temperature (Data in brackets are the corresponding scanning velocities in mm/s) (Li and Yao, 1999)

## 6. Conclusions

Laser forming simulation and experiments are conducted under the condition of constant peak temperature, which largely isolates the effects of strain rate from that of temperature. The high temperature involved makes the strain rate effects on flow stress and thus deformation in the laser forming process quite significant. The bend angle decreased by about 30% for nearly doubled strain rate under the conditions used. Residual stress in the Y direction increased moderately with strain rate. For the nearly doubled strain rate, residual stress increases by about 15% under the conditions used. With the same strain rate increase, the hardness at the irradiated surface of the formed samples decreased by about 7% due to the reduced work hardening.

## Convex Laser Forming

### 1. Introduction

Most investigations have been made for TGM-dominated concave laser forming process. However, there are occasions in practical applications where convex forming is required. Fig. 4.1 shows examples where concave laser bending can not be applied due to impossible access by the laser beam. It has been shown that convex bending is possible under the buckling mechanism (BM), which is induced when the ratio of laser beam diameter to sheet thickness is small, resulting lower through-thickness temperature gradient. A local elastic buckling and plastic deformation takes place as a result of the thermal expansion more or less uniform throughout the sheet thickness (Arnet and Vollertsen, 1995).

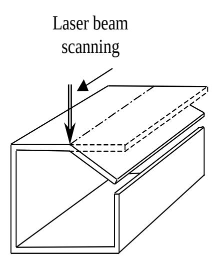


Fig. 4.1 Example requiring convex forming (dash lines indicating the shape before laser

But understandably the direction of the buckling heavily depends on the initial stress and strain state of the sheet. For example, if a sheet is slightly bent, the buckling will take place in the bent direction. In fact, Arnet and Vollertsen (1995) conducted research on convex bending using dependency of bend angle on laser power, scanning velocity and beam diameter for steel (St14), AlMg3 and Cu at different values of thickness. Holzer, et al. (1994) conducted a numerical simulation under a similar condition. Vollertsen, et al. (1995) proposed an analytical model for the BM dominated process. That is $\alpha_b = [36\alpha_{th} k_f Ap / c_P \rho E v s^2]^{1/3}$, where $\alpha_{th}$ is the coefficient of thermal expansion, $k_f$ the flow stress in the heated region, $Ap$ the coupled laser power, $c_p$ the specific heat of the material, $\rho$ the density, $E$ the modulus of elasticity, $v$ the processing speed, $s$ the sheet thickness. The model does not determine the direction of the buckling.

For industrial applications, pre-bending a flat sheet or to heavily constraining a sheet in order to effect convex bending is not economic and sometimes impossible as seen in Fig. 4.1. It is postulated that if the starting point of the laser scanning is at a point other than one on a sheet edge, the direction of buckling will be certain, that is convex. In almost all laser forming work reported to date, laser forming starts from an edge of the sheet. The postulate is based on the fact that although the temperature difference between the top and bottom surface is small under the buckling mechanism, the flow stress is slightly lower and the tendency of thermal expansion is slightly higher at the top surface because of the slightly higher temperature there. The slight difference will be amplified by the heavier mechanical constrains introduced by the non-edge starting point which is completely surrounded by material. As the result, the amplified difference is sufficient to serve as a disturbance to induce buckling to take place in that direction. Once the buckling occurs in that direction, the rest of the forming process will be in that direction. The postulate is validated by the experimental and numerical results to be explained below.

### 2. Experiments

Instead of starting laser scanning at an edge (i.e., $X_s$=0 in Fig. 4.2), a non-zero value of $X_s$ is used for the reasons stated before. A scan starts from a point $X_s$ mm away from the left edge rightward till reaching the right edge. To complete the scan, the scan resumes at a point $X_s$ mm away from the right edge leftward till reaching the left edge. The overlap in scanning is primarily to reduce the so-called edge effect (Bao & Yao, 1999). The parameters used in the experiments are shown in Table 2. The sheet material and experimental procedure are same as above.

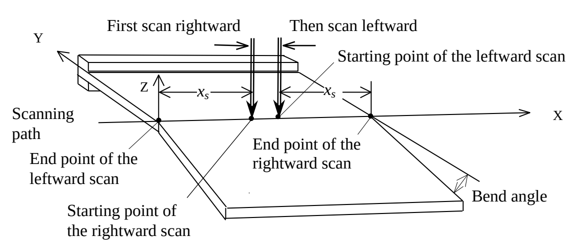


Fig. 4.2 Scanning scheme for convex laser forming

Table 2 Experimental parameters for convex laser forming (Sheet size: 80x80 mm)

| No | Power (W) | Velocity (mm/s) | Diameter (mm) | Thick (mm) |
|---|---|---|---|---|
| 1 | 900 | 30 | 12.0~14.8 | 0.89 |
| 2 | 900 | 20~58.3 | 14.8 | 0.89 |
| 3 | 700 | 18.3~50 | 14.8 | 0.89 |
| 4 | 600~1010 | 30 | 14.8 | 0.89 |
| 5 | 807~1345 | 36.7 | 14.8 | 0.89 |

| | | | | |
|---|---|---|---|---|
| 6 | 600~1200 | 36.7 | 14.8 | 0.61 |

## 3. Theoretical Aspects

For an isotropic material, the relationship between stress $\sigma_{ij}$ and strain $\varepsilon_{ij}$ including the influence of temperature can be written in terms of tensor as

$$\varepsilon_{ij} = \frac{1}{E}[(1+\nu)\sigma_{ij} - \nu\delta_{ij}\sigma_{kk}] + \delta_{ij}\alpha\Delta T \quad (17)$$

where $E$ is the modulus of elasticity, $\nu$ the Poisson's ratio, $\delta_{ij}$ the Kronecker delta, $\alpha$ the coefficient of thermal expansion, and $\Delta T$ the temperature change.

The deflections of the buckled plate is obtained by buckling equation (Thornton, *et al.*, 1994)

$$\Delta\Delta w = \frac{1}{k}\left(N_x^* \frac{\partial^2 w}{\partial x^2} + 2N_{xy}^* \frac{\partial^2 w}{\partial x \partial y} + N_y^* \frac{\partial^2 w}{\partial y^2}\right)$$

$$k = \frac{Eh^3}{12(1-\nu^2)} \quad (18)$$

where $w$ is the deflection of the plate in the $Z$ direction, $h$ is the thickness of the plate, $k$ is the bending stiffness of the plate, $E$ is the modulus of elasticity, $\alpha$ is the coefficient of thermal expansion, $\nu$ is Poisson's ratio, and $\Delta$ is potential operator. $N^*_x$, $N^*_y$, *and* $N^*_{xy}$ are stress resultants, which are given by multiplying the stresses by the plate thickness. The plastic buckling of a plate is governed by

$$\left(1-\frac{3}{4}\lambda\frac{N_x^2}{\overline{N}^2}\right)\frac{\partial^4 w}{\partial x^4} + 2\left(1-\frac{3}{2}\lambda\frac{N_x N_y}{\overline{N}^2}\right)\times$$
$$\times\frac{\partial^4 w}{\partial x^2 \partial^2 y} + \left(1-\frac{3}{4}\lambda\frac{N_y^2}{\overline{N}^2}\right)\frac{\partial^4 w}{\partial y^4} + \quad (19)$$
$$+\frac{N_x}{\overline{D}}\frac{\partial^2 w}{\partial x^2} + \frac{N_y}{\overline{D}}\frac{\partial^2 w}{\partial y^2} + 2\frac{N_{xy}}{\overline{D}}\frac{\partial^2 w}{\partial x \partial y} = 0$$
$$\overline{D} = \frac{E_s s^3}{9}, \lambda = 1 - \frac{E_t}{E_s}$$

where $E_s = \dfrac{\overline{\sigma}}{\overline{\varepsilon}}$ is the secant modulus, $\overline{\sigma}$ the effective stress, $\overline{\varepsilon}$ the effective strain, $\overline{N} = \overline{\sigma}s$, and $E_t$ the tangent modulus.

These equations describe the behavior of the buckling deformation involved in this study. Analytical solutions for the laser forming processes will be difficult to obtain without significant simplifications. Instead, numerical simulation is conducted.

## 4. Numerical Simulation

The assumptions and boundary conditions are similar to previous section. Three-dimensional heat-transfer elements with eight nodes DC3D8 is used for thermal analysis, and continuum stress/displacement elements with the same dimension and number of nodes C3D8 for structure analysis. Temperature-dependent work hardening of the material due to plastic deformation is considered. Strain-rate and temperature effects on flow stress are taken into account

## 5. Results and Discussion

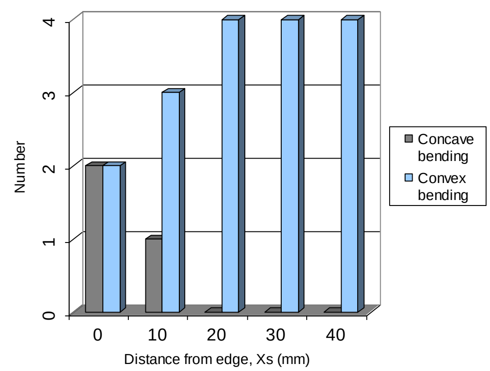


Fig. 4.3 Histogram of bending direction vs. distance from edge, $X_s$ (power:900W, velocity:30mm/s, beam diameter:14.8mm) (Li and Yao, 2000)

Fig. 4.3 is a histogram of bending direction for different distance from edge, $X_s$. When $X_s$=0, i.e., scanning from an edge, the bending direction is uncertain, two samples were bent concavely and two convexly. This is consistent with published results, that is, in a BM-dominated laser forming process, buckling will occur but the direction of the buckling is uncertain and heavily depends on the initial stress/strain state. When $X_s$ increases, i.e., the starting point of the scanning moving away from the edge, the bending becomes predominantly convex. When the starting point approaches the middle of the plate, that is, $X_s$ approaches 40 mm, the bending is always convex. This clearly confirms the postulate made earlier, that is, in a BM-dominated laser forming process there is a slight difference in temperature/thermal expansion between the top and bottom surfaces, the difference is significantly amplified by the added mechanical constraints when the starting point of the scanning moves away from an edge. As a result, material at the starting point starts to buckle convexly. Once the starting point has even a small convex bending, the rest of the forming process will understandably follow its lead. For the rest of the experiments and all simulation studies, $X_s$=25 mm.

The Fourier number, $F_o$, is defined as $F_o = \frac{\alpha_d d}{s^2 v}$, where $\alpha_d$ is the thermal diffusivity, $d$ the beam diameter, $s$ the sheet thickness, $v$ the scanning velocity. Shown in Fig. 4.4 are bending angles at both convex and concave directions when the Fourier number $F_o$ varies from about 6.25 to 7.75. It can be seen that corresponding to small values of the Fourier number, concave bending, represented by a positive value, always occurs even $X_s$=25 mm. When $F_o$ increases, the direction of bending becomes uncertain. Beyond the critical region, convex bending always takes place for the reasons already stated earlier.

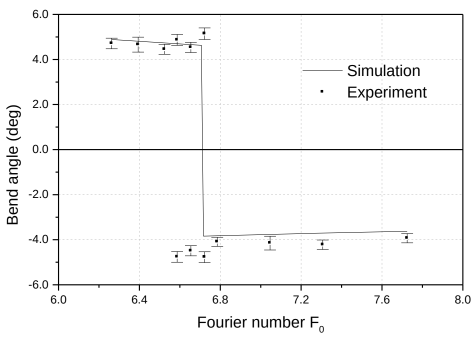


Fig. 4.4 Bend angle vs. Fourier number $F_0$ (power: 900W, velocity: 30mm/s, size: 80×80×0.89mm, diameter: 12-14.8mm) (Li and Yao, 2000)

A typical result of thermal-mechanical simulation of convex laser forming is shown in Fig. 4.5. Fig. 4.5(a) shows temperature distribution and deformation at the beginning of the scan. Fig. 4.5(b) shows a formed sheet that has undergone natural cooling for a few minutes. Comparing it with the un-deformed sheet shown in the same figure, it is obvious that it is convexly bent. It can also be seen that the bending edge is curved (although magnified) and this is because the X-axis plastic contraction near the top surface is larger than that near the bottom surface (Bao and Yao, 1999).

Shown in Fig. 4.6 are comparisons between numerical and experimental results of bending angle vs. power and non-dimensional parameter $v_n$. $v_n$ is defined as $vs/\alpha_d$. Figs 4.4 and 4.6 together show that the simulation results are fairly consistent with the experimental measurements. For obvious reasons, the bending angle becomes more negative with laser power increase, and less negative with velocity increase.

**6. Conclusions**

A new scanning scheme is postulated, in

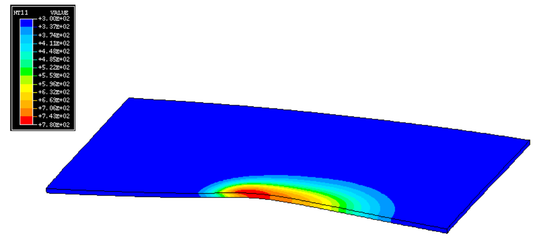

(a) 0.113 second

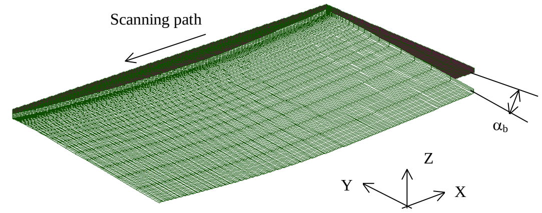


(b) 1000 second

Fig. 4.5 (a) Deformed shape with temperature contour (magnification 5X). (b) Comparison between undeformed sheet (top) and deformed one (bottom) (magnification 3.5X)(showing half plate due to symmetry, power: 800W, velocity: 30mm/s, beam diameter: 14.8mm, size: 80×80×0.89mm)(Li and Yao, 2000)

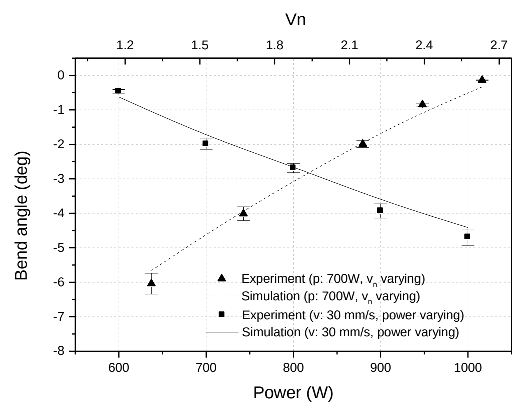


Fig. 4.6 Numerical and experimental results of variation of bend angle with power $p$ and dimensionless velocity $v_n$ (beam diameter: 14.8mm, workpiece size: 80×80×0.89mm) (Li and Yao, 2000)

which laser scanning starts from a location near the middle of workpiece instead of normally from an edge of the workpiece. Using the scanning scheme, convex forming is realized with high certainty unlike the case of scanning from the edge where either concave or convex forming could take place. The postulate is successfully validated by experimental and numerical results. With the method, neither pre-bending nor additional external mechanical constraints are needed in order to effect convex laser forming. Even with the new scanning scheme, the condition for buckling mechanism to dominate still needs to be satisfied. Otherwise, convex forming may not be reliably obtained or not be obtainable at all. In this connection, the Fourier number $F_o$ can be used as a threshold between the concave and convex deformation.

**Authors:** Y. Lawrence Yao is an Associate Professor, Wayne Li a Ph.D. candidate, and Kai Chen a postdoctoral research fellow in the Department of Mechanical Engineering at Columbia University.

## REFERENCES

Alberti, N., Fratini, L., and Micari, F., 1994, "Numerical simulation of the laser bending process by a coupled thermal mechanical analysis," *Laser Assisted Net Shape Eng., Proc. of the LANE'94*, Vol. 1, pp. 327-336.

Arata, Y., *et al*, 1979, "Dynamic behavior in laser gas cutting of mild steel", *Trans. JWRI*, Vol. 8(2), pp.15-26.

Arnet, H., and Vollertsen, F., 1995, "Extending laser bending for the generation of convex shapes," *IMechE Part B: Journal of Engineering Manufacture*, Vol. 209, pp. 433-442.

Bao, J., and Yao, Y. L., 1999, "Analysis and Prediction of Edge Effects in Laser Bending," *Proc. ICALEO '99*, San Diego, Nov., 1999.

Brandt, A. D., and Settles, G. S., 1997, "Effect of nozzle orientation on the gas dynamics of inert-gas laser cutting of mild steel", *J. of Laser Application*, Vol. 9, pp. 269-277.

Chen, K, and Yao, Y. L., 1999, "Striation Formation and Melt Removal in Laser Cutting Process," *J. Manufacturing Processes*, SME, Vol. 1, No. 1, 1999, pp. 43-53.

Chen, K, Yao, Y. L., and Modi, V., 1999a, "Numerical Simulation of Oxidation Effects in Laser Cutting Process," *Int. J. Advanced Manufacturing Technology*, Vol. 15, pp. 835-842.

Chen, K., Yao, Y. L., and Modi, V., 1999b, "Gas Jet - Workpiece Interactions in Laser Machining," *ASME Trans. J. of Manufacturing Science and Engineering,* accepted (1999).

Chryssolouris, G., and Choi, W. C., 1989, "Gas jet effects on laser cutting", *SPIE Vol. 1042 $CO_2$ Lasers and Applications*, pp. 86-96.

Craik, A. D. D., 1966, "Wind-generated waves in thin liquid films", *J. Fluid Mech*., Vol. 26, pp.269-392.

Di Pietro, P., Yao, Y. L., and Chen, K., 1997, "An experimental study of on-line estimation of striations in laser cutting process", *Technical Papers of NAMRI*, pp. 105-110.

Fieret, J., *et al.*, 1987, "Overview of flow dynamics in gas-assisted laser cutting", *SPIE Vol. 801 High Power Lasers*, pp. 243-250.

Hennige, T., Holzer, S., Vollertsen, F., and Geiger, M., 1997, "On the working accuracy of laser bending," *Journal of Materials Processing Technology*, Vol. 71, pp. 422-432.

Holzer, S., Arnet, H., and Geiger, M., 1994, "Physical and numerical modeling of the buckling mechanism," *Laser Assisted Net Shape Eng., Proceedings of the LANE'94*, Vol.1 pp. 379-386.

Hsiao, Y.-C., Shimizu, H., Firth, L., Maher, W., and Masubuchi, K., 1997, "Finite element modeling of laser forming," *Proc. ICALEO '97*, Section A, pp. 31-40.

Ivarson, A., *et al*., 1994, "The oxidation dynamics of laser cutting of mild steel and the generation of striations on the cut edge", *J. of Materials Processing Tech*, Vol. 40, pp. 359-374.

Ivarson, A., *et al*., 1996, "The role of oxygen pressure in laser cutting mild steels", *J. of Laser Applications*, Vol. 8, pp. 191-196.

Li, W., and Yao, Y. L., 1999, "Effects of Strain Rate in Laser Forming," *Proc. ICALEO '99*, San Diego, Nov., 1999.

Li, W., and Yao, Y. L., 2000, "Convex Laser Forming with High Certainty," *Trans. NAMRC XVIII,* May '00, Kensington, KY.

Magee, J., Watkins, K. G., Steen, W. M., 1997, "Edge effects in laser forming," *Laser Assisted Net Shape Engineering 2, Proc. of the LANE'97*, Meisenbach Bamberg, pp. 399-406.

Magee, J., Watkins, K. G., Steen, W. M., 1998, "Advances in laser forming," *Journal of Laser Application*, Vol. 10, pp. 235-246.

Makashev, N. K., "1993, Gas-hydro-dynamics of CW laser cutting of metals in inert gas", *Industrial Lasers and Laser Material Processing, Proc. SPIE*, 2257, pp. 2-9, 1993.

Man, H. C., *et al*., 1997, "Design of supersonic nozzle for laser cutting with pressure gas", *Proc. ICALEO'97*, Sec. B, pp. 118-127.

O'Neill, W. and Steen, W. M., 1995, "A three-dimensional analysis of gas entrainment operating during the laser-cutting process", *J. Phys. D: Appl. Phys.* Vol. 28, 1995, pp.12-18.

O'Neill, W., *et al*., 1992, "The dynamics behavior of gas jets in laser cutting", *Proc. ICALEO'92*, pp. 449-458.

Oosthuizen, P. H., and Carscallen, W. E., 1997, *Compressible Fluid Flow,* The McGraw-Hill Companies, Inc.

Schuocker, D., 1986, "Dynamic phenomena in laser cutting and cut quality", *Appl. Phys*. B, 40, pp.9-14.

Sprenger, A., Vollertsen, F., Steen, W. M., and Watkins, K., 1994, "Influence of strain hardening on laser bending," *Laser Assisted Net Shape Eng., Proc. of the LANE'94*, Vol. 1, pp. 361-370.

Thornton, E. A., Coyle, M. F., and McLeod, R. N., 1994, "Experimental study of plate buckling induced by spatial temperature gradients," *Journal of Thermal Stresses*, Vol. 17, pp. 191-212.

Vicanek, M., *et al*., 1996, "Hydrodynamic instability of melt flow in laser cutting", *J. Phys. D: Appl. Phys*., Vol. 20, pp. 140-145, 1986.

Vollertsen, F., 1994a, "Mechanism and models for laser forming," *Laser Assisted Net Shape Engineering, Proceedings of the LANE'94*, Vol. 1, pp. 345-360.

Vollertsen, F., 1994b, "An analytical model for laser bending," *Laser in Engineering*, Vol. 2, pp. 261-276.

Vollertsen, F., Geiger, M., and Li, W. M., 1993, " FDM and FEM simulation of laser forming a comparative study," *Advanced Technology of Plasticity*, Vol. 3, pp. 1793-1798.

Vollertsen, F., Kome, I., and Kals, R., 1995, "The laser bending of steel foils for microparts by the buckling mechanism- a model," *Modeling Simul. Mater. Sci. Eng*. Vol.3., pp.107-119.